

Hydroxylation of Methane by Non-Heme Diiron Enzymes: Molecular Orbital Analysis of C–H Bond Activation by Reactive Intermediate Q

Mu-Hyun Baik,[†] Benjamin F. Gherman,[†] Richard A. Friesner,^{*,†} and Stephen J. Lippard^{*,‡}

Contribution from the Department of Chemistry, Columbia University, New York, New York 10027, and the Department of Chemistry, Massachusetts Institute of Technology, Cambridge, Massachusetts 02139

Received May 4, 2002

Abstract: The electronic structures of key species involved in methane hydroxylation performed by the hydroxylase component of soluble methane monooxygenase (sMMO), as proposed previously on the basis of high-level density functional theory, were investigated. The reaction starts with initial approach of methane at one of the bridging oxo atoms in intermediate Q, a di(μ -oxo)diiron(IV) unit. This step is accompanied by a proton-coupled outer-sphere transfer of the first electron from a C–H σ -bond in methane to one of the metal centers. The second electron transfer, also an outer-sphere electron transfer process, occurs along a two-component reaction pathway. Both redox reactions are strongly coupled to structural distortions of the diiron core. The electronic consequence and driving force of these distortions are intuitively explained by using the computed Kohn–Sham orbitals in the broken-symmetry framework to incorporate the experimentally observed antiferromagnetic coupling of the unpaired electrons at the metal centers. The broken-symmetry orbital scheme is essential for describing the C–H bond activation process in a consistent and complete manner, enabling derivation of both an intuitive and quantitative understanding of the most salient electronic features that govern the details of the hydroxylation.

Introduction

The selective catalytic hydroxylation of methane to methanol performed by the enzyme methane monooxygenase (MMO) has attracted much attention in the past few years.^{1–4} Substantial progress has been made in both identifying and understanding key features of the catalysis. Structural studies of soluble MMO extracted from *Methylococcus capsulatus* (Bath)^{5–7} and *Methyl- osinus trichosporium* OB3b⁸ have identified the reactive site to be the diiron center of the hydroxylase (MMOH) of the three-component protein system. Although the identity of the key intermediate of the hydroxylation reaction, labeled Q, has been widely agreed upon,^{4,9} its structure has thus far remained largely elusive. Details of the hydroxylation step are similarly not established, although extensive experimental studies have

provided much insight.^{10–25} A number of proposals for the reaction mechanism based on quantum mechanical calculations, mostly using density functional theory (DFT),^{26,27} exist in the

* To whom correspondence should be addressed.

[†] Columbia University.

[‡] Massachusetts Institute of Technology.

- (1) Feig, A. L.; Lippard, S. J. *Chem. Rev.* **1994**, *94*, 759.
- (2) Liu, K. E.; Lippard, S. J. *Adv. Inorg. Chem.* **1995**, *42*, 263.
- (3) Wallar, B. J.; Lipscomb, J. D. *Chem. Rev.* **1996**, *96*, 2625.
- (4) Merckx, M.; Kopp, D. A.; Sazinsky, M. H.; Blazyk, J. L.; Müller, J.; Lippard, S. J. *Angew. Chem., Int. Ed.* **2001**, *40*, 2782.
- (5) Rosenzweig, A. C.; Nordlund, P.; Takahara, P. M.; Frederick, C. A.; Lippard, S. J. *Chem. Biol.* **1995**, *2*, 409.
- (6) Rosenzweig, A. C.; Frederick, C. A.; Lippard, S. J.; Nordlund, P. *Nature* **1993**, *366*, 537.
- (7) Whittington, D. A.; Lippard, S. J. *J. Am. Chem. Soc.* **2001**, *123*, 827.
- (8) Elango, N.; Radhakrishnan, R.; Froland, W. A.; Wallar, B. J.; Earhart, C. A.; Lipscomb, J. D.; Ohlendorf, D. H. *Protein Sci.* **1997**, *6*, 556–568.
- (9) Shu, L. J.; Nesheim, J. C.; Kauffmann, K.; Münck, E.; Lipscomb, J. D.; Que, L. *Science* **1997**, *275*, 515.

- (10) Nordlander, E.; Andersson, K. K. *J. Biol. Inorg. Chem.* **1998**, *3*, 300.
- (11) Deeth, R. J.; Dalton, H. J. *Biol. Inorg. Chem.* **1998**, *3*, 302.
- (12) Whittington, D. A.; Valentine, A. M.; Lippard, S. J. *J. Biol. Inorg. Chem.* **1998**, *3*, 307.
- (13) Shteinman, A. A. *J. Biol. Inorg. Chem.* **1998**, *3*, 325.
- (14) Lipscomb, J. D.; Que, L. *J. Biol. Inorg. Chem.* **1998**, *3*, 331.
- (15) (a) Brazeau, B. J.; Lipscomb, J. D. *Biochemistry* **2000**, *39*, 13503. (b) Brazeau, B. J.; Austin, R. N.; Tarr, C.; Groves, J. T.; Lipscomb, J. D. *J. Am. Chem. Soc.* **2001**, *123*, 11831. (c) Brazeau, B. J.; Wallar, B. J.; Lipscomb, J. D. *J. Am. Chem. Soc.* **2001**, *123*, 10421. (d) Valentine, A. M.; Stahl, S. S.; Lippard, S. J. *J. Am. Chem. Soc.* **1999**, *121*, 3876. (e) Nesheim, J. C.; Lipscomb, J. D. *Biochemistry* **1996**, *35*, 10240. (f) Ambundo, E. A.; Friesner, R. A.; Lippard, S. J. *J. Am. Chem. Soc.* **2002**, *124*, 8770.
- (16) Ruzicka, F.; Huang, D. S.; Donnelly, M. I.; Frey, P. A. *Biochemistry* **1990**, *29*, 1696.
- (17) Priestley, N. D.; Floss, H. G.; Froland, W. A.; Lipscomb, J. D.; Williams, P. G.; Morimoto, H. *J. Am. Chem. Soc.* **1992**, *114*, 7561.
- (18) Liu, K. E.; Johnson, C. C.; Newcomb, M.; Lippard, S. J. *J. Am. Chem. Soc.* **1993**, *115*, 939.
- (19) Lee, S. K.; Fox, B. G.; Froland, W. A.; Lipscomb, J. D.; Münck, E. *J. Am. Chem. Soc.* **1993**, *115*, 6450.
- (20) Lee, S. K.; Nesheim, J. C.; Lipscomb, J. D. *J. Biol. Chem.* **1993**, *268*, 21569.
- (21) Choi, S. Y.; Eaton, P. E.; Kopp, D. A.; Lippard, S. J.; Newcomb, M.; Shen, R. N. *J. Am. Chem. Soc.* **1999**, *121*, 12198.
- (22) Valentine, A. M.; Wilkinson, B.; Liu, K. E.; Komar-Panicucci, S.; Priestley, N. D.; Williams, P. G.; Morimoto, H.; Floss, H. G.; Lippard, S. J. *J. Am. Chem. Soc.* **1997**, *119*, 1818.
- (23) Valentine, A. M.; Tavares, P.; Pereira, A. S.; Davydov, R.; Krebs, C.; Koffman, B. M.; Edmondson, D. E.; Huynh, B. H.; Lippard, S. J. *J. Am. Chem. Soc.* **1998**, *120*, 2190.
- (24) (a) Jin, Y.; Lipscomb, J. D. *J. Inorg. Biochem.* **1999**, *74*, 182. (b) Jin, Y.; Lipscomb, J. D. *Biochemistry* **1999**, *38*, 6178–6186. (c) Jin, Y.; Lipscomb, J. D. *J. Biol. Inorg. Chem.* **2001**, *6*, 717.

literature.^{28–55} Probably as a consequence of the intrinsically complicated nature of the electronic structure (vide infra) encountered in this and similar dinuclear high-spin iron complexes, these proposals offer considerably different mechanistic details. These differences arise from the size of the model, assumptions made to treat the magnetic coupling between the two iron centers, and the number of ligands coordinated to the iron centers. Recently, we^{28,30} proposed a structure for Q based on large-scale quantum mechanical model (~100 atoms) calculations and suggested a mechanism for the hydroxylation of methane. Intermediate Q is generated in the catalytic cycle by reductive activation of dioxygen. To evaluate critically these different proposals, a thorough electronic structure characterization is required that goes beyond descriptions of the structures and reporting of the energies of key intermediates. Conceptual features of the proposed mechanism must be identified that can be used to refine the correlation between theory and experiment.

Systematic molecular orbital (MO) studies that reveal electronic implications of a mechanism are rare and available only for very small, highly simplified models.⁴⁸ In this paper, we present such an intuitively comprehensible analysis of the key electronic features of the previously proposed hydroxylation of methane by intermediate Q.^{28,30} We employ state-of-the-art computational methodology to generate a large-scale model that delivers quantitatively reliable energetics and takes advantage of a molecular orbital analysis that offers a simple rationale for

the chemical driving force of the reaction. The main goal is to understand the function of each reaction step, delineating electron and atom transfer processes, and to elucidate the structure–reactivity relationships for the proposed intermediates. The stereoelectronic description of the two electron transfer steps and characterization of the redox-active intermediates are of special interest and consequently the major achievements of this study.

Computational Details and Theoretical Methods

All calculations are carried out using density functional theory as implemented in the Jaguar 4.1 suite⁵⁶ of ab initio quantum chemistry programs. Geometry optimizations are done with the B3LYP^{57–61} functional and the 6-31G** basis set, where iron is represented by use of the Los Alamos LACVP** basis.^{62–64} The energies of the optimized structures are reevaluated by additional single-point calculations on each optimized geometry by use of Dunning's⁶⁵ correlation-consistent triple- ζ basis set cc-pVTZ(-f) that includes a double set of polarization functions. For iron we have used a modified version of the LACVP**, designated as LACV3P**, where the exponents were decontracted to match the effective core potential with the triple- ζ quality basis.

One of the crucial aspects of many carboxylate-bridged diiron centers is that the unpaired electrons are antiferromagnetically coupled. In principle, multireference methods such as CASSCF are required to describe rigorously the antiferromagnetically coupled spin state, which is impracticable for systems of the present size owing to computational demands. In practice, Noodleman's broken-symmetry (BS) approach,^{66,67} which makes use of the Heisenberg spin operator formalism to obtain a reasonable electronic structure description, has provided a working protocol for single-reference methods, such as DFT, employing the unrestricted spin formalism. We closely follow the protocol described elsewhere³⁰ to obtain the broken symmetry orbitals and use the unrestricted spin formalism in all calculations. The large number of unpaired electrons at the iron core and the intrinsic electronic flexibility of the transition metals give rise to a number of energetically similar electronic states. Therefore, we use spin densities derived from Mulliken population analysis that have also been used in many previous studies^{28–40,49–55} to confirm that the correct, or at least a reasonable, electronic state has been constructed. The use of BS orbitals to describe the intrinsically multiconfigurational problem of antiferromagnetic coupling between iron centers enables a simple and meaningful visualization of the molecular orbitals in a single determinant framework. The localized nature of the metal-based d-orbitals, however, makes it difficult to understand intuitively the details of mixing of atomic orbitals by simple group-theory arguments and the expansion of each MO as symmetry-adapted linear combination (SALC) of atomic orbitals.⁶⁸ The SALC method affords highly delocalized, metal-based atomic orbitals according to the local symmetry at the diiron center, where the respective d-orbitals on each iron atom combine in an in-phase and out-of-phase fashion. The BS orbitals are much more localized on each iron center, however. Although there is usually notable mixing between d-orbitals on different iron centers, the metal-d-dominated MOs can be reasonably approximated as being localized

- (25) (a) Newcomb, M.; Shen, R. N.; Lu, Y.; Coon, M. J.; Hollenberg, P. F.; Kopp, D. A.; Lippard, S. J. *J. Am. Chem. Soc.* **2002**, *124*, 6879. (b) Valentine, A. M.; LeTadic-Biadatti, M. H.; Toy, P. H.; Newcomb, M.; Lippard, S. J. *J. Biol. Chem.* **1999**, *274*, 10771.
- (26) Parr, R. G.; Yang, W. *Density Functional Theory of Atoms and Molecules*; Oxford University Press: New York, 1989.
- (27) Ziegler, T. *Chem. Rev.* **1991**, *91*, 651.
- (28) Gherman, B. F.; Dunietz, B. D.; Whittington, D. A.; Lippard, S. J.; Friesner, R. A. *J. Am. Chem. Soc.* **2001**, *123*, 3836.
- (29) Friesner, R. A.; Dunietz, B. D. *Acc. Chem. Res.* **2001**, *34*, 351.
- (30) Dunietz, B. D.; Beachy, M. D.; Cao, Y. X.; Whittington, D. A.; Lippard, S. J.; Friesner, R. A. *J. Am. Chem. Soc.* **2000**, *122*, 2828.
- (31) Guallar, V.; Gherman, B. F.; Miller, W. H.; Lippard, S. J.; Friesner, R. A. *J. Am. Chem. Soc.* **2002**, *124*, 3377.
- (32) Musaev, D. G.; Basch, H.; Morokuma, K. *J. Am. Chem. Soc.* **2002**, *124*, 4135.
- (33) Torrent, M.; Vreven, T.; Musaev, D. G.; Morokuma, K.; Farkas, O.; Schlegel, H. B. *J. Am. Chem. Soc.* **2002**, *124*, 192.
- (34) Torrent, M.; Musaev, D. G.; Basch, H.; Morokuma, K. *J. Comput. Chem.* **2002**, *23*, 59.
- (35) Basch, H.; Musaev, D. G.; Morokuma, K. *J. Phys. Chem. B* **2001**, *105*, 8452.
- (36) Torrent, M.; Mogi, K.; Basch, H.; Musaev, D. G.; Morokuma, K. *J. Phys. Chem. B* **2001**, *105*, 8616.
- (37) Torrent, M.; Musaev, D. G.; Morokuma, K.; Basch, H. *J. Phys. Chem. B* **2001**, *105*, 4453.
- (38) Basch, H.; Musaev, D. G.; Mogi, K.; Morokuma, K. *J. Phys. Chem. A* **2001**, *105*, 3615.
- (39) Torrent, M.; Musaev, D. G.; Morokuma, K. *J. Phys. Chem. B* **2001**, *105*, 322.
- (40) Basch, H.; Mogi, K.; Musaev, D. G.; Morokuma, K. *J. Am. Chem. Soc.* **1999**, *121*, 7249.
- (41) Yoshizawa, K. *J. Organomet. Chem.* **2001**, *635*, 100.
- (42) Yoshizawa, K.; Suzuki, A.; Shiota, Y.; Yamabe, T. *Bull. Chem. Soc. Jpn.* **2000**, *73*, 815.
- (43) Yoshizawa, K. *J. Biol. Inorg. Chem.* **1998**, *3*, 318.
- (44) Yoshizawa, K.; Shiota, Y.; Yamabe, T. *J. Am. Chem. Soc.* **1998**, *120*, 564.
- (45) Yoshizawa, K.; Ohta, T.; Yamabe, T.; Hoffmann, R. *J. Am. Chem. Soc.* **1997**, *119*, 12311.
- (46) Yoshizawa, K.; Yokomichi, Y.; Shiota, Y.; Ohta, T.; Yamabe, T. *Chem. Lett.* **1997**, 587.
- (47) Yoshizawa, K.; Yamabe, T.; Hoffmann, R. *New J. Chem.* **1997**, *21*, 151.
- (48) Yoshizawa, K.; Hoffmann, R. *Inorg. Chem.* **1996**, *35*, 2409.
- (49) Siegbahn, P. E. M. *J. Biol. Inorg. Chem.* **2001**, *6*, 27.
- (50) Siegbahn, P. E. M.; Crabtree, R. H. *J. Am. Chem. Soc.* **1997**, *119* (9), 3103.
- (51) Siegbahn, P. E. M. *Chem. Phys. Lett.* **2002**, *351*, 311.
- (52) Siegbahn, P. E. M.; Blomberg, M. R. A. *Chem. Rev.* **2000**, *100*, 421.
- (53) Siegbahn, P. E. M. *Inorg. Chem.* **1999**, *38*, 2880.
- (54) Siegbahn, P. E. M.; Crabtree, R. H.; Nordlund, P. *J. Biol. Inorg. Chem.* **1998**, *3*, 314.
- (55) Lovell, T.; Han, W.-G.; Liu, T.; Noodleman, L. *J. Am. Chem. Soc.* **2002**, *124*, 5890.

- (56) Jaguar 4.1: Schrödinger, Inc., Portland, OR, 2000.
- (57) Slater, J. C. *Quantum Theory of Molecules and Solids, Vol. 4: The Self-Consistent Field for Molecules and Solids*; McGraw-Hill: New York, 1974.
- (58) Becke, A. D. *J. Chem. Phys.* **1993**, *98*, 5648.
- (59) Becke, A. D. *Phys. Rev. A* **1988**, *38*, 3098.
- (60) Lee, C. T.; Yang, W. T.; Parr, R. G. *Phys. Rev. B* **1988**, *37*, 785.
- (61) Vosko, S. H.; Wilk, L.; Nusair, M. *Can. J. Phys.* **1980**, *58* (8), 1200.
- (62) Hay, P. J.; Wadt, W. R. *J. Chem. Phys.* **1985**, *82*, 270.
- (63) Wadt, W. R.; Hay, P. J. *J. Chem. Phys.* **1985**, *82*, 284.
- (64) Hay, P. J.; Wadt, W. R. *J. Chem. Phys.* **1985**, *82*, 299.
- (65) Dunning, T. H. *J. Chem. Phys.* **1989**, *90*, 1007.
- (66) Noodleman, L. *J. Chem. Phys.* **1981**, *74*, 5737.
- (67) Yamaguchi, K.; Jensen, F.; Dorigo, A.; Houk, K. N. *Chem. Phys. Lett.* **1988**, *149*, 537.
- (68) Cotton, F. A. *Chemical Applications of Group Theory, 3rd Ed.*; John Wiley & Sons: New York, 1990.

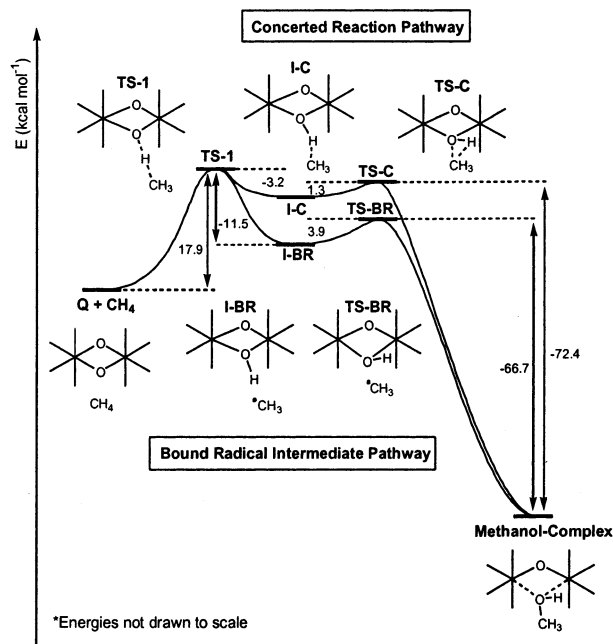


Figure 1. Schematic reaction energy profile of the proposed methane hydroxylation mechanism.

on each of the iron centers. A more detailed and systematic discussion of the differences between the SALC and BS MOs is presented elsewhere.⁶⁹

In this paper, only the BS MOs are presented and highly idealized orbital cartoons are derived by inspection of all atomic orbital coefficients of all high-energy orbitals in each complex. Our previous investigation²⁸ of the MMO system was carried out on a large 100-atom model. To simplify the MO analyses, we truncated the model by removing substituents on the first-shell ligands, replacing glutamate by acetate and histidine by imidazole ligands, thus constructing an approximately 60-atom model. The geometry of these truncated models was not reoptimized, but rather left at that found in the 100-atom model. Both the relative energies and Mulliken spin population changes due to the truncation are fully consistent with the larger model. Thus, we use the spin densities and energies of the 100-atom model, whereas the orbital plots and their respective energies are taken from the truncated model.

Results and Discussion

Figure 1 depicts schematically the proposed reaction energy profile of methane hydroxylation by the MMOH reactive intermediate Q.²⁸ The computed structure of Q (Figure 2) shows two Fe(IV)-d⁴ centers confirmed by Mulliken spin densities of 3.5 with opposite signs⁷⁰ (Table 1) to indicate antiferromagnetic coupling. The iron sites are bridged by two oxo ligands that originate from dioxygen and adopt approximately octahedral local coordination geometry with one bridging and three terminal carboxylates and two histidine ligands. The remaining site on Fe1 is occupied by a water ligand. The terminal histidine and carboxylate groups of Glu144 and Glu209 create different

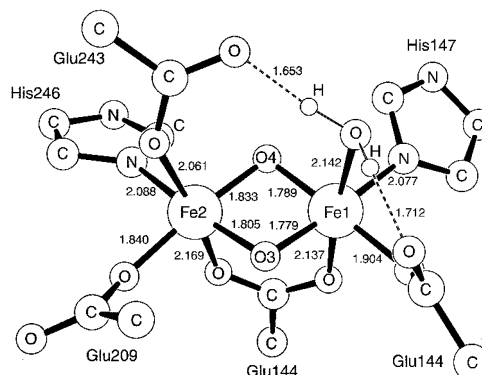


Figure 2. Optimized model structure of Q taken from ref 10. Distances are given in angstroms, and the ligands are labeled according to the peptidyl origins. Note that only the fragments shown are used in the model, thus representing the histidine groups with imidazoles and glutamate moieties with acetate ligands.

Table 1. Mulliken Spin Populations during the Reaction of Q with Methane

species	Fe1	Fe2	O3	O4	H	CH ₃
Q	-3.49	3.54	-0.06	-0.03	n/a	n/a
TS-1	-3.39	4.17	-0.38	-0.28	-0.02	-0.43
IR	-3.38	4.24	0.01	-0.26	-0.02	-0.92
IC	-3.44	4.23	0.04	-0.28	-0.02	-0.87
TSR	-3.49	4.23	0.10	-0.22	0.00	-0.94
TSC	-3.44	4.23	0.04	-0.28	-0.02	-0.82
methanol complex	-4.17	4.20	-0.01	-0.15	0.00	0.00

chemical environments for the bridging oxo ligands, which has a profound effect on the reactivity (vide infra). Overall, the methane hydroxylation reaction is a two-electron redox process with each of the Fe(IV) centers formally accepting one electron from the methyl carbon atom, which becomes formally oxidized in the process and ultimately forms a carbon–oxygen bond.

The first, rate-determining step involves nucleophilic attack of methane head-on at the bridging oxo group labeled as O3 in Figure 2, with concomitant electron transfer from the C–H σ -bond to Fe2, probably via O3. The transition state, TS-1, which is located at a relative energy of 17.9 kcal/mol from the reactant, has a linear O···H···C arrangement typical for a concerted, proton-coupled electron-transfer reaction.⁷¹ The Mulliken spin density analysis (Table 1) indicates that the first electron transfer is nearly completed at this stage. After TS-1 is traversed, two slightly different reaction pathways are possible. The first involves the formation of a bound methyl radical intermediate designated as the recoil/rebound mechanism and labeled as the bound radical intermediate pathway in Figure 1. The methyl group does not detach from the hydroxyl moiety in what is labeled the concerted pathway in Figure 1. In both cases, the reaction requires an upward rotation of the newly formed H–O bond. Unlike the first electron transfer, the second electron transfer is late and there is no indication of electron transfer at the transition states TS-BR or TS-C. In both transition states the spin population analysis reveals a typical Fe(IV) center and substantial radical character on the methyl moiety. Once the second transition state is traversed, the electron transfer accompanied by C–O bond formation occurs along the exothermic reaction path in a barrierless fashion, regardless of the pathway taken.

(69) Baik, M.-H.; Lee, D.; Friesner, R. A.; Lippard, S. J. *Isr. J. Chem.* **2001**, *41*, 173.

(70) The spin densities of 3.5 on each iron center are indicative of high-spin ($S = 2$) configurations. A second reasonable possibility is an intermediate-spin ($S = 1$) state with only half of the four d-electrons unpaired on each metal center. A recent computational study (ref 55) has shown that the $S = 1$ spin state of the antiferromagnetically coupled Q is 7.53 kcal/mol higher in energy than the $S = 2$ state. This result is in good agreement with typical values found in exploratory calculations for our large-scale model. Thus, this alternative is not further considered.

(71) Hrovat, D. A.; Borden, W. T. *J. Am. Chem. Soc.* **1994**, *116*, 6459.

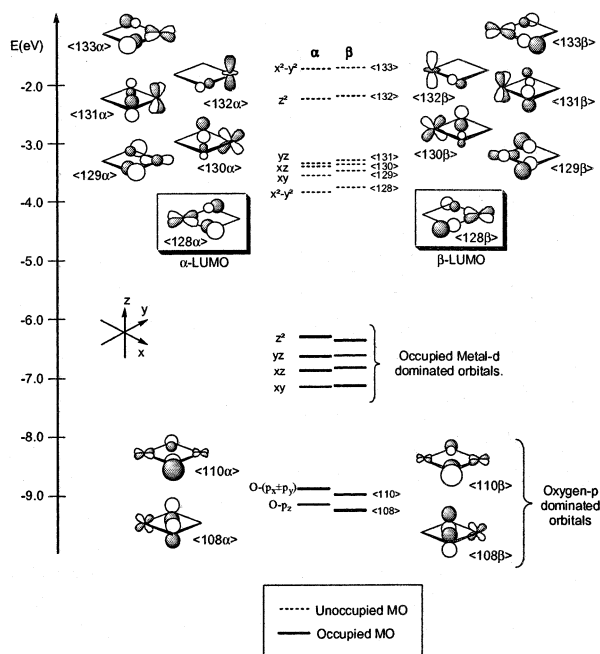


Figure 3. Simplified partial MO diagram of Q. Cartoon representations of selected orbitals are drawn. In the cartoons, the main atomic orbital characters of the MOs are exaggerated and smaller contributions are neglected for clarity.

In the following, we examine electronic features that promote the first electron transfer, which is the most difficult step of the C–H bond activation. The redox-active orbitals will be identified and tracked along the course of the reaction. In the second part, we concentrate on the upward rotation of the hydroxo bridge, which apparently determines the barrier height of the second electron transfer.

MO Diagram of Q. Figure 3 shows a schematic MO diagram of the antiferromagnetically coupled model of Q with BS orbitals. Note that BS orbitals are derived from orbitals that were first localized on each of the iron centers. They do not show the expected shapes of SALC orbitals⁶⁹ that one might write down approximating the local structure of the dimer as D_{2h} , in which case highly delocalized in-phase and out-of-phase combinations of the appropriate metal d-orbitals would arise. Instead, the high degree of localization displayed by BS orbitals allows the distribution of α - and β -electrons relatively independently of one another, avoiding the creation of electronic structures with unoccupied orbitals energetically below the highest occupied molecular orbital (HOMO), which would render the DFT wavefunction invalid.²⁶ The most important molecular orbitals are those dominated by metal d-orbitals, which are usually nonbonding or metal–ligand antibonding frontier orbitals. There are 5 metal d-orbitals for each iron center, giving rise to 10 MOs that need to be considered. Since we make use of the unrestricted spin formalism, where the α - and β -orbitals are treated separately, there are 20 spin MOs that are of significant interest. If the d^4 -Fe(IV) centers are coupled antiferromagnetically, one can expect four occupied α -orbitals that are dominated by metal d atomic orbitals of one iron center and four occupied β -orbitals dominated by atomic orbitals centered at the other metal center. The remaining six orbitals for each set of spin orbitals remain empty. All 20 orbitals are depicted in Figure 3. In addition, two of the occupied lone-pair orbitals centered at the bridging oxo groups are also drawn,

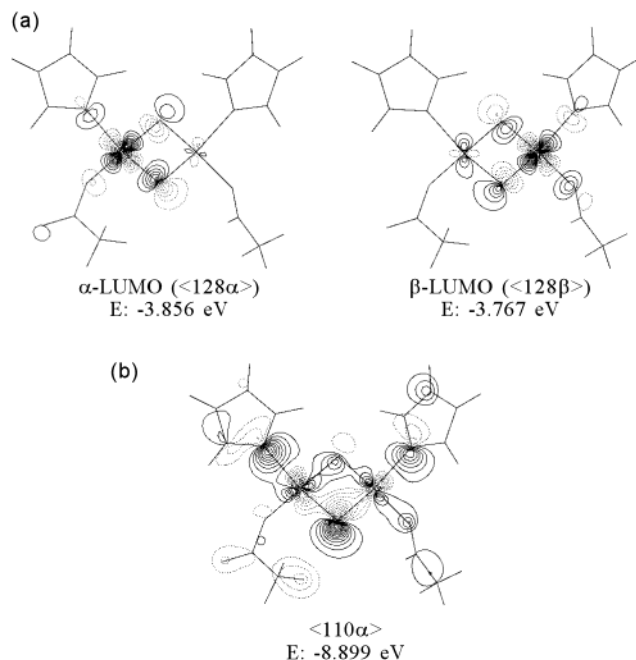


Figure 4. Contour plot (contour interval 0.05 au) of selected Q-MOs: (a) α/β -LUMO (b) redox-active O3 lone-pair orbital ($\langle 110\alpha \rangle$).

since they play a key role in the electron-transfer reaction (vide infra). These MOs contain minor contributions from metal d-orbitals, which are important for the electron transfer. Thus, the metal-based orbital characters are indicated in Figure 3, although the oxygen-based atomic orbitals are highly dominant.

The ordering of the metal-based MOs depicted in Figure 3 is very easy to understand if the approximate octahedral ligand field around each iron center is considered and the dimer is envisioned as two independent octahedra that are arranged in an edge-sharing fashion. At the given orientation of the dimer with the x - and y -axes approximately aligned along the Fe–O bonds, the atomic orbitals d_{xy} , d_{xz} , and d_{yz} form a t_{2g} -like set, whereas d_{z^2} and $d_{x^2-y^2}$ form the e_g -like set. Not surprisingly, the t_{2g} -like orbitals are lower in energy than the e_g -like orbitals. The energy splitting that the set of unoccupied orbitals shown in Figure 3 displays resembles the familiar Dq splitting of a simple octahedral complex. Most important for the reaction pathway are the lowest unoccupied molecular orbitals (LUMO) of both the α - and β -spin orbitals. These redox-active MOs will be utilized to accept the two electrons transferred subsequently from the substrate to the Fe_2O_2 core. Contour plots of these important spin orbitals are shown in Figure 4a. The α -LUMO ($\langle 128\alpha \rangle$) is an iron $d_{x^2-y^2}$ dominated orbital mostly located on Fe2, whereas the β -LUMO ($\langle 128\beta \rangle$) is the corresponding orbital centered at Fe1. Note that the contour plots show that the localization of the BS orbitals is not perfect and some mixing of d-orbitals from both iron centers can be seen. For simplicity, the cartoon representations (Figure 3) only show the major contributions in an exaggerated fashion.

In general, the more strongly electron-withdrawing Glu243 carboxylate ligand on Fe2 compared to the water ligand on Fe1 gives rise to slightly lower orbital energies of the MOs centered on Fe2. Consequently, the α -LUMO is energetically lower by 0.09 eV than the β -LUMO, predicting that the first electron transferred to the Fe_2O_2 core should be more stable at Fe2, as is proposed in our mechanism. In previous work²⁸ we explored

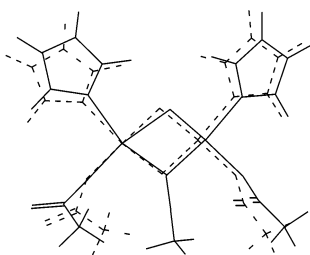


Figure 5. Overlaid structure traces of Q (broken line) and TS-1 (solid line). Axial ligands are not shown.

many possible directions of initial nucleophilic attack of methane and concluded the head-on approach at the bridging oxo moiety was the only energetically viable pathway. The shape of the LUMO reveals an intuitive reason for this finding. According to frontier orbital theory,^{72–75} the initial nucleophilic attack occurs at the highest amplitude of the Fukui(+) function, which can be approximated⁷⁶ by squaring of the LUMO. Thus, the most intuitive site for an initial nucleophilic attack is at O3 and in a planar alignment with the Fe₂O₂ plane. Figure 5 compares the computed structure of the transition state TS-1 with that of Q. With the above considerations and the assumption that the structural relaxation following the initial attack is moderate, the transition-state geometry can be understood intuitively. The directionality of the α -LUMO orbital on O3 suggests that a nonorthogonal attack of the nucleophile with respect to the iron-iron vector is preferable. The Fe–O antibonding character of α -LUMO also infers an elongation of both Fe2–O3 and Fe2–O4 bonds upon electron transfer, as confirmed in transition state TS-1, where the Fe2–O3 and Fe2–O4 distances increase by 0.165 and 0.259 Å, respectively.²⁸

First Electron Transfer. One of the most important questions for the first step of the reaction is the exact mechanism of electron transfer. The alignment of the substrate with the α -LUMO suggests direct transfer from methane via the oxo bridge to the iron center by use of the α -LUMO $\langle 128\alpha \rangle$. The Fe(IV) center is a highly efficient oxidant, requiring only one additional electron to achieve a half-filled d-shell configuration. The oxidation of methane is very demanding, however, and the question arises naturally whether an Fe(IV) center surrounded by fairly electron-rich ligands is intrinsically able to oxidize methane. If the first electron transfer occurs simply by direct coupling of the substrate with the α -LUMO via the O3 bridge to the metal, which would be a classical example of an outer-sphere electron transfer moderated by delocalization of the metal-based acceptor orbital into a tightly bound ligand, one expects β -electron density build-up at the methyl moiety due to α -electron loss and, consequently, an increase of α -electron density at Fe2 with residual α -electron traces on O3. The Mulliken spin density distributions for Q and TS-1, given in Table 1, show the expected increase of α -spin density at Fe2 from 3.54 to 4.17, values routinely computed for Fe(IV) and Fe(III) centers, respectively. The grouped spin densities of the CH₃ moiety also display the expected behavior and become more negative, which by convention indicates an excess of β -electrons. The spin density at O3 becomes substantially more

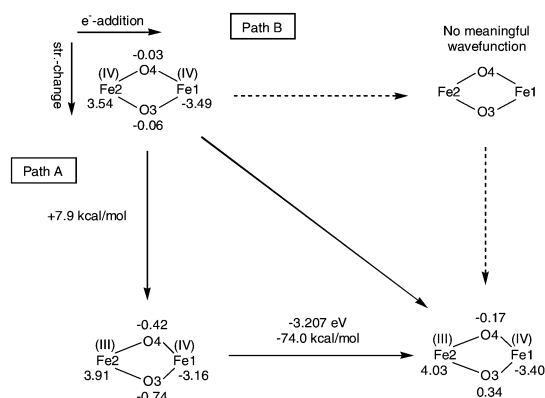


Figure 6. Computational square scheme. The Mulliken spin densities and the formal oxidation states that are most consistent with the spin densities are given at each metal center. The magnitude of structural distortion is exaggerated for clarity.

negative by 0.32, however, from -0.06 in Q to -0.38 in TS-1. Such an increase of β -electron density at O3 is inconsistent with a simple α -electron-transfer mechanism from substrate to the metal center.

To explain this surprising electron density flux, it is necessary to examine the Fe₂O₂ core distortion in more detail. As shown in Figure 5, there is a significant structural change of the Fe₂O₂ core upon methane addition, as briefly mentioned above. Structural distortions triggered by redox processes are very common phenomena and can be formally decomposed into structural and electronic components.^{77,78} The first step of this decomposition protocol is to distort the structure of Q from its equilibrium geometry to that found in TS-1 without providing a substrate or an electron. Then a separate single-point calculation at the same distorted structure is performed, adding one α -electron to the system. Figure 6 summarizes the results of this decomposition, labeled as path A. The second possibility, where the electron is added to the equilibrium structure of Q without allowing structural change, is also shown for completeness (path B in Figure 6). Path B promises an interesting evaluation of the intrinsic reduction potential of Q without structural distortion. We were, however, unable to obtain a stable and meaningful wavefunction for the one-electron-reduced system at the geometry of Q. This instability of the wavefunction suggests a very strong coupling between structural distortion and the redox process. We concentrate on path A in the following analysis.

The structural distortion of the Fe₂O₂ core from the equilibrium geometry of Q to that found at TS-1, which is energetically uphill by 8 kcal/mol, has a profound effect on the spin density distribution. The elongation of the Fe2–O3/O4 bonds alone, without any consideration of a substrate or an electron source, triggers an intramolecular electron transfer from O3 to Fe2, giving rise to an α -electron density of 3.91 at Fe2, which is more consistent with an Fe(III) than with an Fe(IV) center. We have labeled Fe2 accordingly in Figure 6. This α -electron transfer creates a significant spin polarization at O3 resulting in a Mulliken spin density of -0.74 , which resembles a radical with almost a full β -electron. The same trend, although to a

(72) Fukui, K. *Science* **1982**, *218*, 747.

(73) Fukui, K.; Koga, N.; Fujimoto, H. *J. Am. Chem. Soc.* **1981**, *103*, 196.

(74) Hoffmann, R.; Imamura, A.; Zeiss, G. D. *J. Am. Chem. Soc.* **1967**, *89*, 5215.

(75) Woodward, R. B.; Hoffmann, R. *J. Am. Chem. Soc.* **1965**, *87*, 395.

(76) Page 99 in ref 26.

(77) Baik, M.-H.; Ziegler, T.; Schauer, C. K. *J. Am. Chem. Soc.* **2000**, *122*, 9143.

(78) Baik, M.-H.; Schauer, C. K.; Ziegler, T. *J. Am. Chem. Soc.* **2002**, *124*, 11167.

much lesser extent, is also observed for O4. The computed spin density of -0.42 indicates that the oxo ligand in the trans position to the two equatorial imidazole ligands is much more sensitive to the structurally induced spin polarization effect.⁷⁹ The electronic structure deformation is again easily understandable from the schematic MO diagram. The relevant lone-pair orbitals of the oxo bridge, $\langle 108 \rangle$ and $\langle 110 \rangle$, are depicted in Figure 3.⁸⁰ Upon structural distortion, orbital $\langle 110\alpha \rangle$ mixes with the α -LUMO, leading to an increase of metal character in the occupied orbital. The oxygen character of the α -LUMO is increased, providing an efficient pathway for intramolecular electron transfer from the in-plane lone-pair orbital $\langle 110\alpha \rangle$ to the α -LUMO.

The next step in our computational square diagram simulates the injection of one α -electron to the Fe_2O_2 core. The addition of a free α -electron overcompensates the spin polarization at O3 to give a spin density of 0.34 . The spin polarizations of Fe1 and O4 also normalize to -3.40 and -0.17 , respectively, which is best viewed as a simple β -electron exchange between Fe1 and O4. The added electron resides essentially entirely on O3, indicating a very local electrophilic nature of the putative intermediate. It is important to note that we are not suggesting that path A depicted in Figure 6 has a real physical meaning. Clearly, the electron-transfer process cannot be envisioned to be decoupled completely from structural changes. The scheme presented here is simply a tool to explore the electronic impact of the structural distortion.

With this electron polarization scheme in mind, the initially counterintuitive increase of β -spin polarization at O3 upon substrate binding and α -electron transfer between the fully optimized Q and TS-1 becomes easy to understand. The Fe_2O_2 core distortion polarizes the O3 center, giving it an excess of β -electrons and increasing its affinity for α -electrons. Upon substrate binding, the O3 center replenishes its α -electron by oxidizing the substrate. Thus, although the overall electron transfer is clearly outer-sphere, the mechanism is not classical, and a push-and-pull process must be considered to explain the differential electron spin density distribution between Q and TS-1.

From this picture, a proposed role of the metal centers in the enzymatic reaction emerges naturally. A radicaloid oxygen center is undesirable in a real environment since it would give rise to a variety of very unspecific reactions. The intimate coupling of spin polarization at O3 and the Fe_2O_2 core distortion allows the creation of radicaloid oxygen character in situ, once the substrate is bound at the active site. The square scheme in Figure 6 also demonstrates that the first redox step must be proton-coupled, since the diiron core without the proton assistance is not powerful enough to oxidize methane. The total reaction energy of -3.207 eV shown in Figure 6 translates to

(79) This interesting relationship between structure and reactivity might be an exploitable design feature. A more detailed quantitative analysis of the chemical difference between O3 and O4 is not helpful for this paper and will be presented elsewhere together with a possible exploitation strategy in synthetic models.

(80) In the Fe_2O_2 core, only half of the oxygen-based lone pairs are shown. Since there are two O(-II) fragments present, there are 2×4 lone pair electrons to consider, which mix with each other as shown in Figure 3. MO $\langle 110 \rangle$ is the out-of-phase combination of $\text{O}3-(p_x \pm p_y)$ with $\text{O}4-(p_x \pm p_y)$ whereas MO $\langle 108 \rangle$ is the in-phase combination of $\text{O}3-p_z$ with $\text{O}4-p_z$. These two orbitals are chosen because they have the right phase to promote the electron transfer.

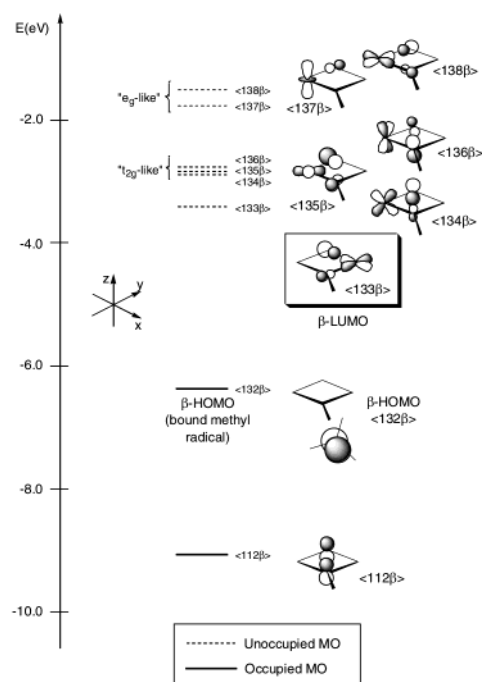


Figure 7. Simplified partial MO diagram of I-BR. Only β -orbitals are drawn and the four occupied metal d-based orbitals are omitted for clarity. The orbital energies are drawn to the same scale as in Figure 3. The methyl-fragment orbitals do not mix with any of the MOs shown in the diagram and thus the methyl skeleton is not shown except for the β -HOMO, which is entirely located on the methyl fragment.

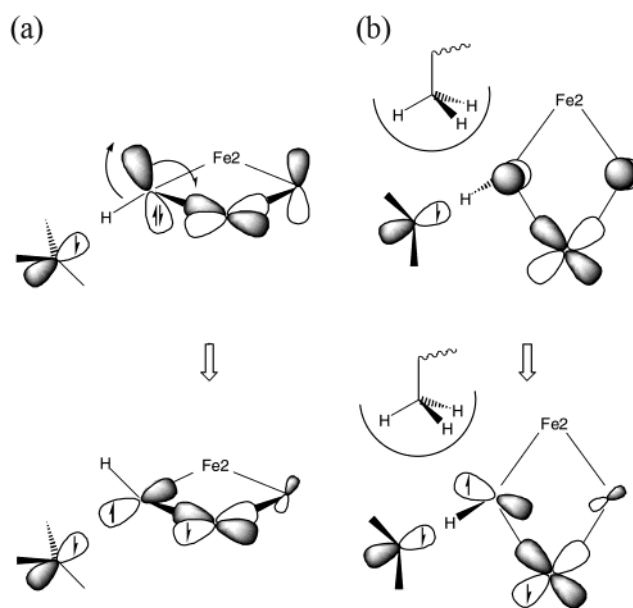


Figure 8. Schematic illustration of the second electron-transfer pathway coupled to the upward rotation of the hydroxyl bridge. Two views of the same process related by a 90° rotation around the O3–O4 vector are shown.

a standard redox potential E_{SHE}^0 of -1.223 V,⁸¹ which is clearly too negative to promote methane oxidation. Thus, proton coupling is not surprisingly immensely important for the

(81) Baik, M.-H.; Friesner, R. A. *J. Phys. Chem. A* **2002**, *106*, 7407. To relate energy differences computed for one-electron redox reactions to standard redox potentials, the simple relationship $\Delta G = -FE^0$ can be used, where F is the Faraday constant and E^0 is the absolute potential. E^0 can be converted to E_{SHE}^0 , the potential referenced to standard hydrogen electrode (SHE), by subtracting the experimentally determined absolute potential of SHE (Reiss, H.; Heller, A. *J. Phys. Chem.* **1985**, *89*, 4207.).

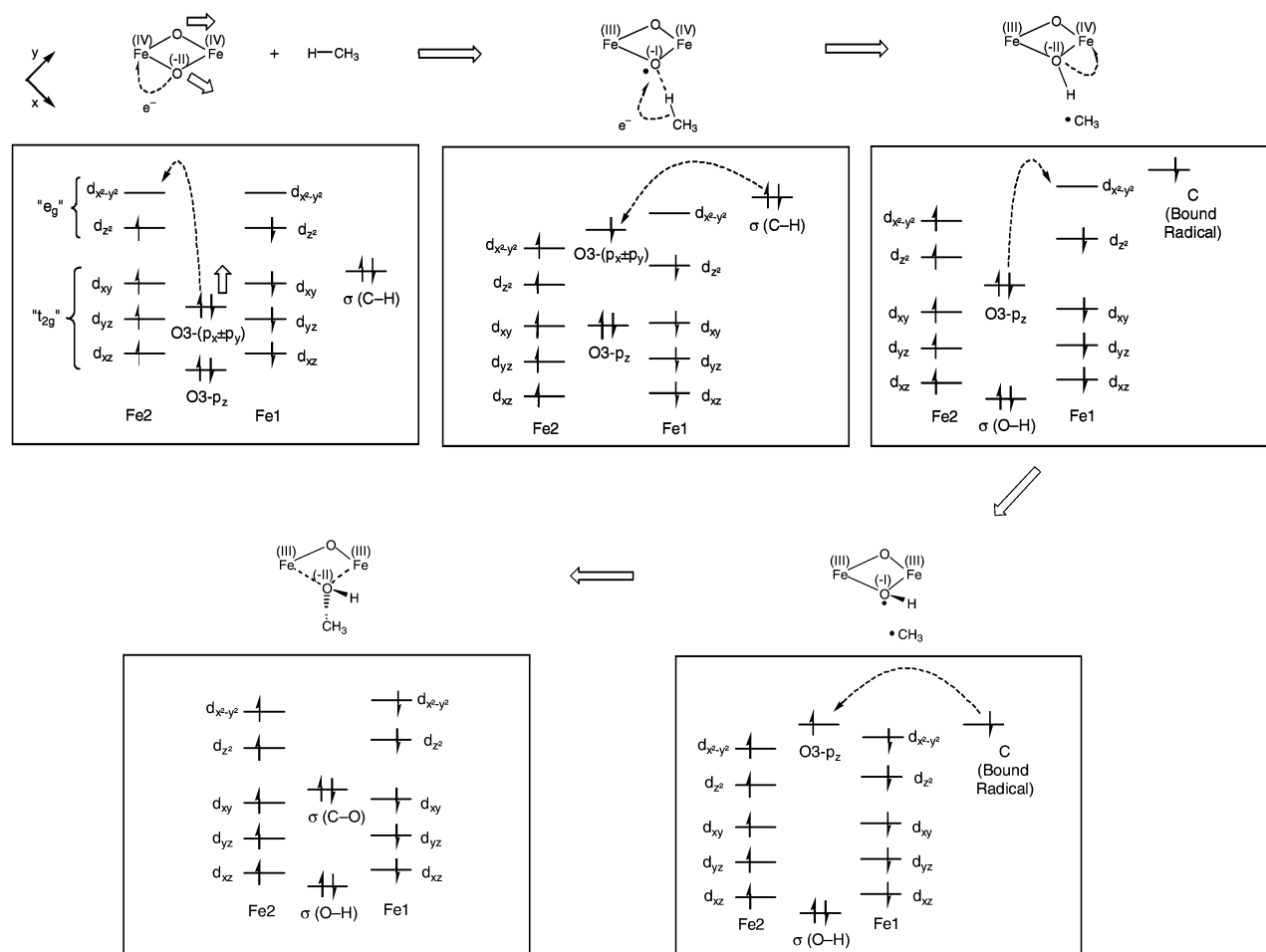


Figure 9. Schematic MO diagram of Q and the transition state of the hydrogen abstraction step showing the necessary electron transfer processes. The orbital energies are not drawn to scale and are only intended to show the qualitative pattern.

thermodynamics of the first electron transfer. A more quantitative assessment of the energy component attributed to proton coupling is not straightforward, since the transfer to O3 is not complete at the transition state.

Second Electron Transfer. To complete the hydroxylation once the transition state TS-1 is traversed, the second electron has to be transferred from the methyl moiety to Fe1, which is formally still a d^4 Fe(IV) center as the Mulliken spin density analysis of TS-1 (Table 1) confirms. Our previously reported calculations revealed two possible channels for the final step. One involves the formation of a radical intermediate in a recoil/rebound mechanism and the other proceeds in a concerted fashion without the methyl moiety detaching completely from the hydroxyl group. We have also assessed recently the probabilities of both channels in a molecular dynamics simulation.³¹ The most salient feature of both pathways is an upward rotation of the newly formed hydroxide group, which is solely responsible for the small barrier computed for the second step. Electron transfer itself is highly exothermic, but there is no evidence that any electron transfer takes place at the second transition states TS-C and TS-BR. Thus, the second electron transfer differs substantially from the first. Whereas the first electron transfer is an early process directly coupled to the structural distortion at the transition state TS-1, the second electron transfer is late and the transition states TS-C and TS-BR are both dominated by structural distortion only without

electron transfer. In the final section of this paper, we examine why the hydroxyl group has to rotate at all and whether there is an electronic reason for this structural change. Intuitively, one could imagine that the upward rotation has the sole purpose of allowing better access to O3 for the methyl group, which needs to form a C–O bond to complete the hydroxylation reaction.

MO Diagram of I-BR. Figure 7 shows a simplified MO diagram of the bound radical intermediate I-BR, where only the most important β -orbitals are drawn. The α -orbitals do not play an important role for the second electron transfer, although they are of course also affected by the structural change. From the expected 10 metal-dominated β -orbitals, four are occupied as seen for Q (not drawn in Figure 7), leaving six metal-based β -MOs unoccupied. Five ($\langle 134\beta \rangle$ – $\langle 138\beta \rangle$) form a complete subset of d-orbitals and maintain the intuitively understandable splitting into the e_g -like and t_{2g} -like sets, with a few insignificant differences arising from the structural change, such as energetic reordering of the t_{2g} -like orbitals when compared to the MO diagram of Q. The β -LUMO, $\langle 133\beta \rangle$, is essentially identical to that in Q. It is easily recognized as mainly Fe1 $d_{x^2-y^2}$ in character. The contributions of O3-based atomic orbitals are slightly decreased compared to Q owing to a lowering of the O3 fragment orbitals upon proton addition to the oxo group. The β -HOMO of I-BR is not surprisingly the methyl carbon p-orbital that contains the unpaired electron.

Figure 8 depicts schematically the second electron-transfer process accompanied by C–O bond formation. The electron transfers from β -HOMO to β -LUMO, leading to C–O bond formation by a bound radical recombination mechanism. The highest occupied orbital with substantial O3 atomic character, $\langle 112\beta \rangle$, is depicted in Figure 7. It is easily recognized as one of the lone-pair orbitals originating from the O3 p_z atomic orbital. Unlike the first electron transfer, there is only poor orbital overlap between $\langle 112\beta \rangle$ and β -LUMO. These orbitals are approximately orthogonal, explaining the need for the upward rotation of the hydroxyl bridge. This rotation maximizes the overlap between the O3 lone pair and the Fe1-based LUMO. In addition, the structural change orients the O3 lone pair toward the bound methyl radical orbital. Since the Fe1 center is only susceptible toward β -electrons, the electron deformation creates a spin-matched polarization at O3 that readily allows bound radical recombination to give the methanol product. It is noteworthy that the lone-pair orbital on O3 that is redox-active for the second electron transfer is also approximately orthogonal to the electron-donating orbital on the methyl radical moiety. This electronic picture is very different from that encountered for the first electron transfer, where the lone pair on O3 was well aligned for interaction with the incoming substrate.

The last notable feature is the directionality of the electron-accepting metal-based orbital, which favors alignment of the mediating O3 lone-pair orbital with the Fe1–O3 axis, as illustrated in Figure 8b. As a consequence, there is a chemical incentive for migration of the bound methyl radical to form an approximately linear arrangement with the Fe1–O3 axis. In our model, this approach is sterically hindered by the methyl fragment of the terminally bound acetate group (Figure 5, solid line), which represents a glutamate moiety (Glu209) found in the enzymatic environment. Note that for the first electron-transfer step the H–C bond was aligned along the Fe2–O3 axis. The consequence of this electronic detail is straightforward. Without the steric hindrance the upward rotation of the hydroxide is expected to be directly connected to methyl migration, resulting in a better orbital alignment that would give

rise to electron transfer at the transition state. In a recent report,⁴⁹ the glutamate moiety was modeled by using a terminally bound formate and a transition state was proposed that clearly shows an approximately linear alignment of the methyl carbon with the Fe1–O3 axis. Consequently, significant electron transfer occurs at the transition state, in disagreement with our results, where no such electron transfer is seen.

Conclusions and Outlook

Figure 9 summarizes schematically the molecular orbital picture of the hydroxylation mechanism discussed above. The molecular orbital and Mulliken spin density analyses suggest that the first electron transfer occurs between the C–H σ -orbital and the O3 ($p_x \pm p_y$) orbital. The latter is prepared for oxidation of the substrate by intramolecular α -electron density flux to Fe2, effecting an overall outer-sphere proton-coupled electron transfer from substrate to Fe2. For the second electron transfer a similar mechanism is operative. The second O3 lone-pair orbital, mostly comprising the p_z atomic orbital, interacts with the second iron center Fe1. Coupling between the electron-donor orbital at the bound methyl radical moiety and the metal center is maximized by an upward rotation of the hydroxide bridge, giving a fully delocalized orbital pathway between donor and acceptor orbitals.

In this account we have discussed only the portion of the catalytic cycle that leads to formation of methanol from methane and activated dioxygen performed by MMOH. The first part of the enzymatic reaction, which affords Q by dioxygen activation starting with the reduced state of MMOH, must also be understood on a similar level of detail as presented here to complete the picture. Efforts to extend our computational model in that direction are currently underway.

Acknowledgment. This work was supported by grants from the NIH to R.A.F. (GM40526) and to S.J.L. (GM32134) and by the National Computational Science Alliance (Grant MCA95C007N; Resource SGI/CRAY Origin2000)

JA026794U